

# New-generation photosensitizer-anchored gold nanorods for a single near-infrared light-triggered targeted photodynamic–photothermal therapy

Zongjunlin Liu<sup>a\*</sup>, Fang Xie<sup>b\*</sup>, Jun Xie<sup>a\*</sup>, Jianhao Chen<sup>b</sup>, Yang Li<sup>c</sup>, Qin Lin<sup>b</sup>, Fanghong Luo<sup>a</sup> and Jianghua Yan<sup>a</sup>

<sup>a</sup>School of Medicine, Anti-Cancer Center, Xiamen University, Xiamen, China; <sup>b</sup>Department of Radiation Oncology, Xiamen Cancer Center, The First Affiliated Hospital of Xiamen University, School of Medicine, Xiamen University, Xiamen, China; <sup>c</sup>Xiamen Institute of Rare Earth Materials, Institute of Haixi, Chinese Academy of Sciences, Xiamen, China

## ABSTRACT

Traditional combined photodynamic and photothermal therapy (PDT/PTT) was limited in clinical treatment of cancer due to the exceptionally low drug delivery efficiency to tumor sites and the activation by laser excitation with different wavelengths. We have accidentally discovered that our synthesized chlorin e6-C-15-ethyl ester (HB, a new type of photosensitizer) be activated by a laser with an excitation wavelength of 660 nm. Herein, we utilized Au nanorods (AuNRs) as 660 nm-activated PTT carriers to be successively surface-functionalized with HB and tumor-targeting peptide cyclic RGD (cRGD) to develop HB-AuNRs@cRGD for single NIR laser-induced targeted PDT/PTT. The HB-AuNRs@cRGD could be preferentially accumulated within tumor sites and rapidly internalized by cancer cells. Thereby, the HB-AuNRs@cRGD could exhibit amplified therapeutic effects by producing both significant reactive oxygen species (ROS) and hyperthermia simultaneously under the guidance of fluorescence imaging. The tumor inhibition rate on ECA109 esophageal cancer model was approximately 77.04%, and the negligible systematic toxicity was observed. This study proposed that HB-AuNRs@cRGD might be a promising strategy for single NIR laser-induced and imaging-guided targeted bimodal phototherapy.

## ARTICLE HISTORY

Received 13 May 2021  
Revised 13 July 2021  
Accepted 19 July 2021

## KEYWORDS






Phototherapy; esophageal cancer; chlorin e6-C-15-ethyl ester; Au nanorods; cRGD

## 1. Introduction

As a safe modality of tumor ablation, phototherapy has received widespread attention for their favorable efficacy in cancer therapy (Baldea et al., 2016; Li et al., 2020; Yang et al., 2021). Two main approaches are available: photodynamic therapy (PDT), which could induce cell apoptosis and necrosis by converting laser energy to generate cytotoxic reactive oxygen species (ROS) under laser irradiation (Mehraban & Freeman, 2015; Kwiatkowski et al., 2018; Donohoe et al., 2019), and photothermal therapy (PTT), which could result in localized irreversible thermal damage to cells by converting laser energy to produce hyperthermia, accompanied by protein denaturation and membrane destruction (Kennedy et al., 2011; Melancon et al., 2011; Yang et al., 2013). Compared with conventional chemotherapy, phototherapy has significant advantages such as the low invasiveness, high spatio-temporal selectivity, and rapid post-operation recovery (Cheng et al., 2014; Li et al., 2020). Therefore, researchers have proposed a new treatment model which is based on the combination of PDT and PTT, exhibiting the better anti-tumor effect via photodynamic and photothermal therapy (PDT/PTT) synergy (Camerin et al., 2016; Denkova et al., 2018).

However, traditional combination of PDT and PTT generally needs to be activated by two separate lasers with different excitation wavelengths, which result in the prolongation of treatment time and the complication of therapeutic process. In particular, if there is a time interval between PDT and PTT, the hyperthermia produced during PTT would accelerate the necrosis of tumor tissue, impeding its absorption of laser and ultimately limiting the efficacy of PDT (Tian et al., 2011; Xiao et al., 2013; Camerin et al., 2016). Therefore, it is necessary to develop a nanoplatform irradiated by a single wavelength laser to generate ROS and hyperthermia, triggering PTT and PDT simultaneously.

In our previous studies, we had developed a new type of photosensitizer, called chlorin e6-C-15-ethyl ester (HB) (Figure 1(A)), which needs to be triggered by a laser with an excitation wavelength of 660 nm (Liu et al., 2020). It could not only be applied to PDT but also shows a good performance in fluorescence imaging and lower dark toxicity. Gold-nanoparticles could not only effectively deliver the HB to tumors by the enhanced permeability and retention (EPR) effect but also effectively convert laser energy to generate hyperthermia to kill tumor cells (Liu et al., 2018a,b,c; Kalyane et al., 2019; Mioc et al., 2019). Importantly, its active intermediate products during PTT could promote the

**CONTACT** Jianghua Yan  [jhyan@xmu.edu.cn](mailto:jhyan@xmu.edu.cn); Fanghong Luo  [luofanghong@xmu.edu.cn](mailto:luofanghong@xmu.edu.cn)  School of Medicine, Anti-Cancer Center, Xiamen University, Xiamen, Fujian, China; Qin Lin  [linqin05@163.com](mailto:linqin05@163.com)  Department of Radiation Oncology, Xiamen Cancer Center, The First Affiliated Hospital of Xiamen University, School of Medicine, Xiamen University, Xiamen, Fujian, China

\*These authors contributed equally to this work.

This article has been corrected with minor changes. These changes do not impact the academic content of the article.

© 2021 The Author(s). Published by Informa UK Limited, trading as Taylor & Francis Group.

This is an Open Access article distributed under the terms of the Creative Commons Attribution-NonCommercial License (<http://creativecommons.org/licenses/by-nc/4.0/>), which permits unrestricted non-commercial use, distribution, and reproduction in any medium, provided the original work is properly cited.

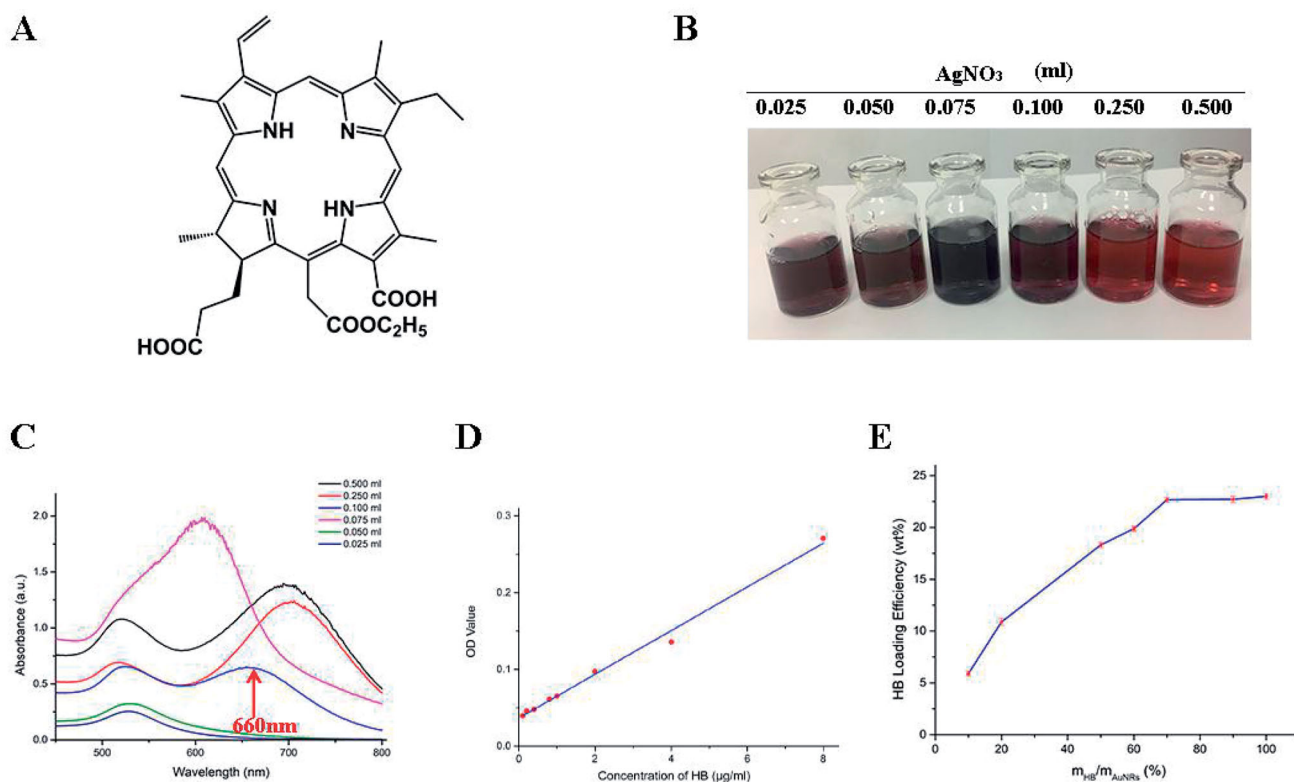


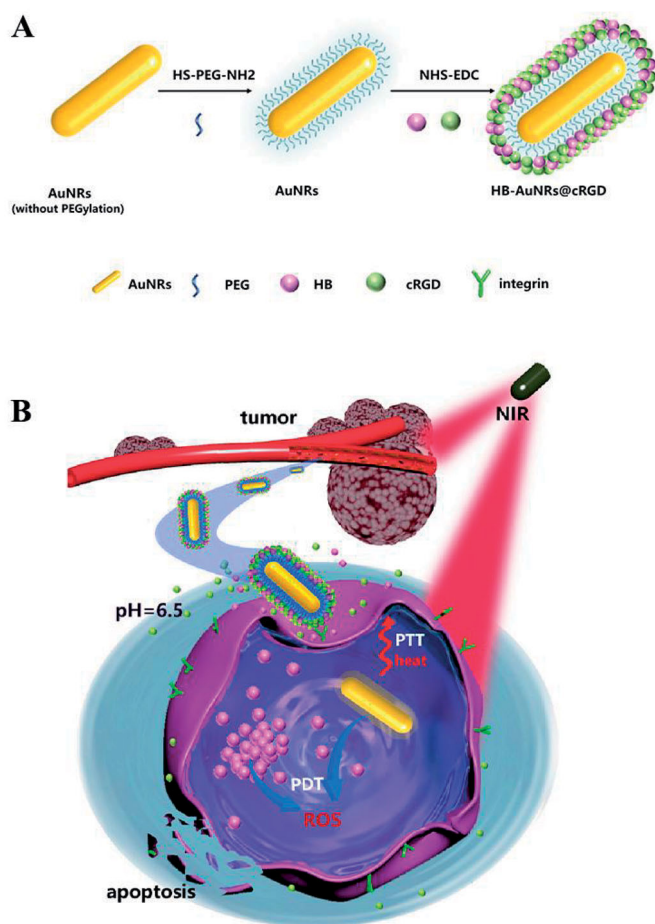
**Figure 1.** Synthesis of HB-AuNRs@cRGD. (A) Schematic diagram of HB structure. (B) Photographs and (C) UV absorption spectrum of AuNRs prepared by adding different concentrations of  $\text{AgNO}_3$ . (D) Standard curve of HB concentration in ultrapure water. (E) HB-loading efficiency of HB-AuNRs@cRGD as a function of different mass ratio of HB/AuNRs.

decomposition of  $\text{H}_2\text{O}_2$  inside tumor cells to produce ROS (Xu et al., 2012a,b; Mohammadi et al., 2013). Therefore, we tried to integrate HB and gold nanorods (AuNRs) into a theranostic nanoplatform, which could achieve PDT and PTT effects simultaneously through only a single NIR laser irradiation (Wang et al., 2013a,b; Li et al., 2017).

However, the tumor-selectivity of these nanoparticles needs to be further improved. The active targeting strategy has been extensively utilized to deliver nanoparticles to tumor cells (Bertrand et al., 2014; Li et al., 2018). It was reported that integrin  $\alpha\text{v}\beta3$  is highly expressed on the surface of most tumor cells and tumor neovascular endothelial cells, but almost not expressed in normal endothelial cells and tissues, which could also inhibit the tumor cell adhesion, proliferation, invasion, and metastasis (Weber et al., 2016; Lino et al., 2019). Arginine (R)-glycine (G)-aspartate (D) (RGD), which could bind to  $\alpha\text{v}\beta3$  integrin with high affinity, was one of the most widely applied peptide sequence for stimulating cell adhesion on synthetic nanodrugs surfaces. Once RGD was recognized and bound to integrins, an integrin-mediated cell adhesion process would be initiated, and subsequently the signal transduction would be activated to influence cell biological behavior. Recently, many emerging studies confirmed nanodrugs composed of RGD and AuNRs could effectively accumulate at the tumors through both EPR and active binding, meanwhile exhibiting highly selective targeting and destructive effects on tumors under NIR laser irradiation (Li et al., 2010; Gui & Cui, 2012; Xu et al., 2012a,b; Liu et al., 2018a,b,c). Inspired by this, we introduced the

cyclic RGD (cRGD, Arg-Gly-Asp-D-Phe-Lys) peptide synthesized by genetic engineering technology and functionalized it on our nanoprobe's surface. Compared with the traditional linear RGD, cRGD possesses more adhesion sites and stronger binding affinity to integrin  $\alpha\text{v}\beta3$ , which is easier to induce apoptosis of tumor cells and inhibit their adhesion and migration (Wang et al., 2013a,b; Kim et al., 2018; Gajbhiye et al., 2019).

Herein, an activatable photosensitizer-introduced theranostic nanoprobe was successfully designed for single NIR laser-induced combined PDT/PTT under the guidance of fluorescence imaging. First, we synthesized AuNRs via the seed-mediated growth method followed by PEGylation. The PEG-modified AuNRs had been found to have long lasting circulation in the blood with low cytotoxicity (Huang et al., 2010; Gui & Cui, 2012). Subsequently, the AuNRs were covalently anchored with HB, and further grafted with a tumor-targeting peptide cRGD to develop HB-AuNRs@cRGD. After intravenous injection of HB-AuNRs@cRGD in ECA109 esophageal tumor-bearing mice, HB-AuNRs@cRGD were efficiently accumulated at the tumor sites via EPR effects, and internalized by tumor cells via cRGD receptor-mediated endocytosis. Once excited by a single 660nm NIR laser, the HB-AuNRs@cRGD would simultaneously produce ROS and hyperthermia, ultimately obtaining an optimal performance of PDT and PTT (Scheme 1). Both results of *in vitro* and *in vivo* experiments showed that compared with the single PDT or single PTT, our nanoprobe can achieve better synergistic antitumor effects under the guidance of fluorescence imaging of HB.



**Scheme 1.** (A) Schematic illustrations of formation of HB-AuNRs@cRGD. (B) Mechanism of combined photothermal (PTT) and photodynamic therapy (PDT) by a single 660 nm laser irradiation.

## 2. Materials and methods

### 2.1. Materials

HB was provided by Haining Lvsheng Pharmaceutical Technology Co., Ltd. (Haining, China). Cetyltrimethylammonium bromide (CTAB), sodium borohydride (NaBH<sub>4</sub>), chloroauric acid (HAuCl<sub>4</sub>), ascorbic acid, N-hydroxysuccinimide (NHS), 1-(3-dimethylaminopropyl)-3-ethylcarbodiimide hydrochloride (EDC), HS-PEG-NH<sub>2</sub> (MW, 2000), and DPBF were purchased from Sigma-Aldrich (Shanghai, China). Silver nitrate (AgNO<sub>3</sub>) was purchased from Shanghai Shenbo Chemical Co., Ltd. (Shanghai, China). c(RGDfK) was purchased from Gil Biochemical Co., Ltd. (Shanghai, China) in the following sequence: Arg-Gly-Asp-D-Phe-Lys. The FITC fluorescent probe was modified at the N-terminus of cRGD, which was purchased from Abcam (Shanghai, China). The cell cytotoxicity kit for CCK-8 assay, calcein AM/PI co-staining, and Annexin V-FITC/PI staining assay were purchased from Shanghai Yisheng Biotechnology Co., Ltd. (Shanghai, China). ROS assay kit (DCFH-DA) for cell, frozen section and Hoechst-33258 were purchased from Abcam (Shanghai, China). Crystal violet for colony formation assay was purchased from Shanghai Biyantian Biological Technology Co. Ltd. (Shanghai, China). Matrigel for Transwell assay was purchased from Becton, Dickinson and Company (Franklin Lakes, NJ). All the used agents were of analytical

grade. In addition, human esophageal cancer cells (ECA109) were obtained from the Cancer Research Center of Xiamen University (Xiamen, China). The female BALB/c mice (4–5 weeks of age, 18–20 g) were purchased from Xiamen University Experimental Animal Co., Ltd. (Xiamen, China).

### 2.2. Synthesis of HB-AuNRs@cRGD

AuNRs were synthesized according to the seed-mediated method (Mehraban & Freeman, 2015). First, we prepared the seed solution by adding NaBH<sub>4</sub> solution (0.60 mL, 0.01 M) into a mixture solution composed of HAuCl<sub>4</sub> (0.10 mL, 0.01 M) and CTAB (7.50 mL, 0.10 M). This seed solution reacted for 2 h. Second, we prepared a growth solution by adding ascorbic acid (0.64 mL, 0.10 M) into a mixture containing HAuCl<sub>4</sub> (1.65 mL, 0.01 M), AgNO<sub>3</sub> (0.10 mL, 0.01 M), and CTAB (95.00 mL, 0.10 M). Third, 0.40 mL of seed solution was added into all the growth solution, and the reaction mixture was allowed to react for 5 h. The product was purified by centrifugation at 8000 rpm for 25 minutes. The resulting blue-black precipitate was dispersed in 100 mL of ultra-pure water.

To obtain the amine-functionalized AuNRs (AuNRs-NH<sub>2</sub>), HS-PEG-NH<sub>2</sub> (10.00 mL, 10.00 μM, MW, 2000) was added and kept stirring overnight. After centrifugal purification, NHS (0.45 mL, 0.10 M) was added into a mixture solution consisting of HB (0.86 mL, 16.00 mM), cRGD (0.02 mL, 0.05 M), and EDC (1.50 mL, 0.10 M), and the reaction mixture was reacted for 12 h. Then, all the products were added into the above 100 mL solution (AuNRs-NH<sub>2</sub>). The reaction mixture was reacted for 48 h and subjected to centrifugal purification.

### 2.3. Characterization of HB-AuNRs@cRGD

Each synthesis step was preliminary monitored by solution appearances, and further confirmed by particle size and zeta potential (Dynamic Light Scattering Particle Size Analyzer SZ-100, Shanghai, China), UV-vis spectra (Agilent Cary 60 UV-Visible Spectrophotometer, Shanghai, China), and fluorescence spectra (PerkinElmer LS55 Fluorescence Spectrophotometer, Waltham, MA) methods. The gold concentration of formulations was measured by inductively coupled plasma mass spectroscopy (ICP-MS, Agilent, Santa Clara, CA). This experiment mainly detected the loading efficiency of HB. After centrifugation, the supernatant was collected and its UV-vis absorbance at 660 nm was used to determine HB. The morphology of nanocarriers was characterized by transmission electron microscopy (TEM, Hitachi HT-7800, Tokyo, Japan) and atomic force microscopy (AFM, Cypher S).

### 2.4. In vitro efficacy evaluation

The solubility of substances in the reaction process and the releasing efficiency of HB under different conditions were evaluated. Samples were irradiated with a 660 nm laser at a power density of 300 mW/cm<sup>2</sup> for different time to achieve photothermal conversion. Real-time thermal imaging of

formulations was recorded by an infrared thermal imaging camera.

### 2.5. Singlet oxygen ( $^1O_2$ ) and mitochondrial membrane potential detection

Under the condition of pH 6.5, HB-AuNRs@cRGD was irradiated under a 660 nm laser to trigger the generation of ROS. The absorbance of the solution containing DPBF (0.01 mM) and HB-AuNRs@cRGD at 415 nm was monitored at determined time points using UV-vis spectrophotometer. The decrease of the absorbance caused by photobleaching of DPBF indicated  $^1O_2$  generation.

In the cell system, we used the DCFH-DA and JC-1 probes to detect  $^1O_2$  generation and mitochondrial membrane potential, respectively. ECA109 cells were incubated with HB, AuNRs, and HB-AuNRs@cRGD (6.40  $\mu$ M HB equiv.) for 24 h with 660 nm laser irradiation (light dose density of 20 J/cm<sup>2</sup>). DCF was monitored by a Leica TCS SP5 CLSM (Wetzlar, Germany) with the excitation and emission wavelengths of 485 nm and 525 nm. Additionally, under the same excitation laser at 488 nm, JC-1 monomer and JC-1 aggregates were detected at the emission wavelengths of 530 nm (green) and 590 nm (red), respectively. The operation should be carried out at a dark environment.

### 2.6. Subcellular localization

ECA109 cells were plated at least 12 h at a density of  $5 \times 10^5$  cells/mL before incubation with HB, AuNRs, and HB-AuNRs@cRGD (6.40  $\mu$ M HB equiv.) for 24 h. Then, 0.5 mL DAPI was added to stain nucleus. The samples were detected by Leica TCS SP5 CLSM (Wetzlar, Germany) to evaluate subcellular localization of HB and cRGD-FITC. HB was monitored by CLSM with the excitation and emission wavelengths of 506 and 663 nm, respectively. cRGD-FITC was monitored by CLSM with the excitation and emission wavelengths of 494 and 518 nm, respectively. DAPI was monitored by CLSM with the excitation and emission wavelengths of 340 and 488 nm, respectively. Flow cytometry fluorescence quantitative analysis was used to detect the cellular uptake of HB. The operation should be consisted in a dark environment.

### 2.7. In vitro phototoxicity studies

ECA109 cells were plated at least 12 h at a density of  $5 \times 10^5$  cells/mL before incubation with HB, AuNRs, and HB-AuNRs@cRGD at serial concentrations of 0, 0.80, 1.60, 3.20, 6.40, and 12.80  $\mu$ M (HB equiv.) for 24 h. After removing non-internalized formulations, the cells were submitted to a 660 nm NIR irradiations at a power density of 120 mW/cm<sup>2</sup> for 84 s or 168 s (light dose density of 10 or 20 J/cm<sup>2</sup>) or no laser conditions, further incubated for 12 h. The cytotoxicity was measured by CCK-8, calcein AM/PI co-staining, and Annexin V-FITC/PI staining assay. All the experiments were conducted in the dark. The cell viability was calculated by using the formula:

$$1 - \frac{OD_{\text{treatment}} - OD_M}{OD_{\text{control}} - OD_M} \times D_{\text{nr}}$$

### 2.8. Wound-healing assay

ECA109 cells were seeded and transiently transfected with HB, AuNRs, and HB-AuNRs@cRGD (3.20  $\mu$ M HB equiv.) for 24 h. Then the cells were submitted to a 660 nm NIR irradiation at the power density of 120 mW/cm<sup>2</sup> for 168 s (light dose density of 20 J/cm<sup>2</sup>) or no laser condition. When cells reached approximately 100% confluency, use a 200  $\mu$ L pipette tip to form a linear wound on the confluent cell layer. Next, the cells were washed twice by PBS, and the culture was continued for 24 h. Then, wound healing was recorded under the inverted microscope. The wound closure rate (%) was calculated by using the formula ( $S_{0h}$  or  $S_{24h}$ : the acreage of the blank area between cells at 0 h or 24 h):

$$1 - \frac{S_{24h}}{S_{0h}} \times \text{hhr}$$

### 2.9. Colony formation assay

ECA109 cells were seeded into 60 mm dishes at a density of  $1 \times 10^3$  cells and incubated with HB, AuNRs, and HB-AuNRs@cRGD (3.20  $\mu$ M HB equiv.) for 24 h. The light irradiation treatment was the same as above. Then, cells were further cultured for 10 d. After being fixed, cell colonies were subsequently stained with 0.5% crystal violet. Then, we used the following formula to calculate the clone formation rate ( $S_1$ : the amount of cell clones,  $S_0$ : the total amount of cells):

$$\frac{S_1}{S_0} \times 100\%$$

### 2.10. Transwell assay

Tumor cell migration and invasion assay were carried out using transwell chambers with 6.5 mm diameter polycarbonate filters (8  $\mu$ m pore size) coated with 35  $\mu$ L Matrigel. The ECA109 cell suspensions ( $1 \times 10^5$ ) in serum-free medium were added to the upper well of transwell chambers, and at the same time 500  $\mu$ L of medium supplemented with 10% FBS was added to the bottom chambers as a chemoattractant. HB, AuNRs, and HB-AuNRs@cRGD (3.20  $\mu$ M HB equiv.) were added to both upper and lower wells. The light irradiation treatment was the same as above. Then, the plates were further cultured for 24 h and the cells on the upper surface of the filter were wiped with a cotton swab. Cells migrating through the filters were fixed, stained with 0.5% crystal violet, and counted under a light microscope.

### 2.11. In vivo phototoxicity studies

All procedures of animal study were approved by the Institutional Animal Care and Use Committee of Xiamen University. The subcutaneous esophageal cancer models were established by injecting 100  $\mu$ L of ECA109 cells suspension ( $1 \times 10^7$  cells/mL) into the right armpit of BALB/c female nude mice (6–8 mice per group). Until the tumors volume reached approximately 100–150 mm<sup>3</sup>, the mice were i.v. administrated with 200  $\mu$ L of free HB, AuNRs, and HB-AuNRs@cRGD (1 mg/kg HB equiv.). For phototherapy studies, 660 nm NIR irradiations at the power density of 200 mW/cm<sup>2</sup> for 500 s (light dose density of 100 J/cm<sup>2</sup>) or no laser

provided 12 h after injection. After phototherapy, the tumor size and body weights were measured every three days. Tumor volume was calculated with the formula:  $V=A \times B^2 \times 1/2$ , where  $A$  is the longest axis and  $B$  is the perpendicular shorter tumor axis. Mice were sacrificed by cervical dislocation at day 15. Tumor tissues and major organs were removed and then fixed in 4% formalin. H&E staining was carried out to monitor the morphological feature of each tissue. Moreover, blood samples of mice were collected for serum chemistry (AST, ALT, CRE) and hematological parameters analysis ( $n=3$ ).

### 2.12. In vivo fluorescence imaging

For the laser-induced *in vivo* fluorescence imaging studies, the tumor-bearing nude mice were injected with 200  $\mu$ L of free HB and HB-AuNRs@cRGD at the same concentration of HB via the tail vein, respectively. The fluorescence imaging was acquired an IVIS Lumina imaging system at different time points. At 12 h post-injection, the mice were sacrificed and the organs and tumor tissues were excised for fluorescence imaging and semi-quantitative analysis ( $n=3$ ).

### 2.13. In vivo infrared thermal imaging

For *in vivo* infrared thermal imaging studies, the tumor-bearing nude mice were injected with 200  $\mu$ L of free PBS, free HB, AuNRs, and HB-AuNRs@cRGD at the same concentration of HB via the tail vein, respectively. A 660 nm laser irradiation (light dose density of 100 J/cm<sup>2</sup>) was applied to the central part of the tumor at 12 h post-injection. An IR camera (Ax5, Beijing, China) was used to measure the temperature rise in tumor tissues during the radiation process to record thermal images in real time ( $n=3$ ).

### 2.14. Statistical analysis

Statistical analyses were carried out using SPSS 24.0 software (SPSS Inc., Chicago, IL), with Student's *t*-test for two groups or one-way ANOVA for multiple groups. All results were expressed as 'mean  $\pm$  SD'. Means were considered significantly different when  $p < .05$ .

## 3. Results and discussion

### 3.1. Synthesis and characterization of HB-AuNRs@cRGD

The AuNRs could be successfully synthesized according to the seed-mediated growth method. Due to the difference of AgNO<sub>3</sub> concentration in the reaction system, the optical properties of AuNRs are also different. By changing the concentration of AgNO<sub>3</sub> (0.10 mL, 0.01 M), we adjusted the optimal UV-vis absorption wavelength of AuNRs to 660 nm, which is consistent with that of HB (Figure 1(B,C)). Thus, a single wavelength of 660 nm laser could be applied to simultaneously excite both HB and AuNRs to exert the effect of PDT/PTT. In addition, according to HB concentration ( $C$ ) and UV-vis absorbance at 660 nm (OD), a standard curve of HB

concentration in ultrapure water ( $OD = 0.0285C + 3.66E-2$ ) was constructed with a linear correlation coefficient ( $R^2=0.9912$ ) (Figure 1(D)). By measuring the UV-vis absorbance of the supernatant at 660 nm, the unloaded HB concentration could be calculated to obtain the loading efficiency of HB. To obtain the optimal HB loading efficiency, we used different mass ratios of HB and AuNRs (mHB/mAuNRs) to prepare nanoprobles. As mHB/mAuNRs was increased, the HB loading efficiency increased linearly. When mHB/mAuNRs was increased to 70%, the HB loading efficiency arrived at about 22.6%. As mHB/mAuNRs continued to increase, the HB loading efficiency showed a slow increase and arrived a plateau (Figure 1(E)). Therefore, we chose 70% HB loading efficiency as the optimal formula ratio, aiming to reduce the HB dosage to obtain the same or better PDT effect.

RGD had been employed extensively owing to their efficient binding capacity to the  $\alpha v \beta 3$  integrin which was frequently overexpressed on both intratumoral neovascular endothelium and tumor cells (Danhier et al., 2012). In previous studies, Miller and Veale confirmed that overexpressed  $\alpha v \beta 3$  integrin was shown for each of the five human esophageal cells maintained *in vitro* and *in vivo* environment (Miller & Veale, 2001). Zheng et al. also found that  $\alpha v \beta 3$  integrin was highly expressed in many tumors including osteosarcomas, melanomas, carcinomas of esophagus and more (Zheng et al., 2014). Consistent with the above results, Tanaka et al. indicated that the overexpression of  $\alpha v \beta 3$  integrin was exhibited in human esophageal carcinomas, which might play an important role in esophageal tumor invasion (Tanaka et al., 2000). Moreover, Fan et al. verified that the tumor tissues in esophageal cancer patients also presented increased expression of integrin  $\alpha v \beta 3$  in both vasculature and cancer cells like other solid tumors (Fan et al., 2018). Therefore, it was an objective fact that esophageal cancer exhibited enhanced expression of integrin  $\alpha v \beta 3$ . Meanwhile, RGD presented superior affinity to the overexpressed  $\alpha v \beta 3$  integrin subunits and effective internalization into esophageal cancer cells for increased tumor homing and cellular uptake (Ruoslahti et al., 2010; Hamzah et al., 2011; Fan et al., 2018). In addition, cyclic peptides could withstand proteolysis and possess more adhesion sites and stronger binding affinity to integrin receptors (Wang et al., 2013a,b; Gajbhiye et al., 2019). In view of the above excellent properties of cRGD and its high binding affinity with  $\alpha v \beta 3$  integrin, we chose this peptide moiety to coat on HB-AuNRs (termed as HB-AuNRs@cRGD) to improve their esophageal tumor targeting capability.

The UV-vis spectra of HB, AuNRs, and HB-AuNRs@cRGD was compared (Figure 2(A)). The characteristic peaks of HB and AuNRs were both at 660 nm, and the payload of HB contributed to the broaden absorption of near-infrared range around 660 nm due to the increased thickness of AuNRs outer shells. Moreover, FITC fluorescent probe was modified in the N terminal of cRGD, in order to identify cRGD. The fluorescence characteristic peaks of FITC in cRGD were observed between 490 nm and 500 nm suggesting successful payload of cRGD. Meanwhile, the fluorescent signal and appearance of HB also changed after being absorbed on the

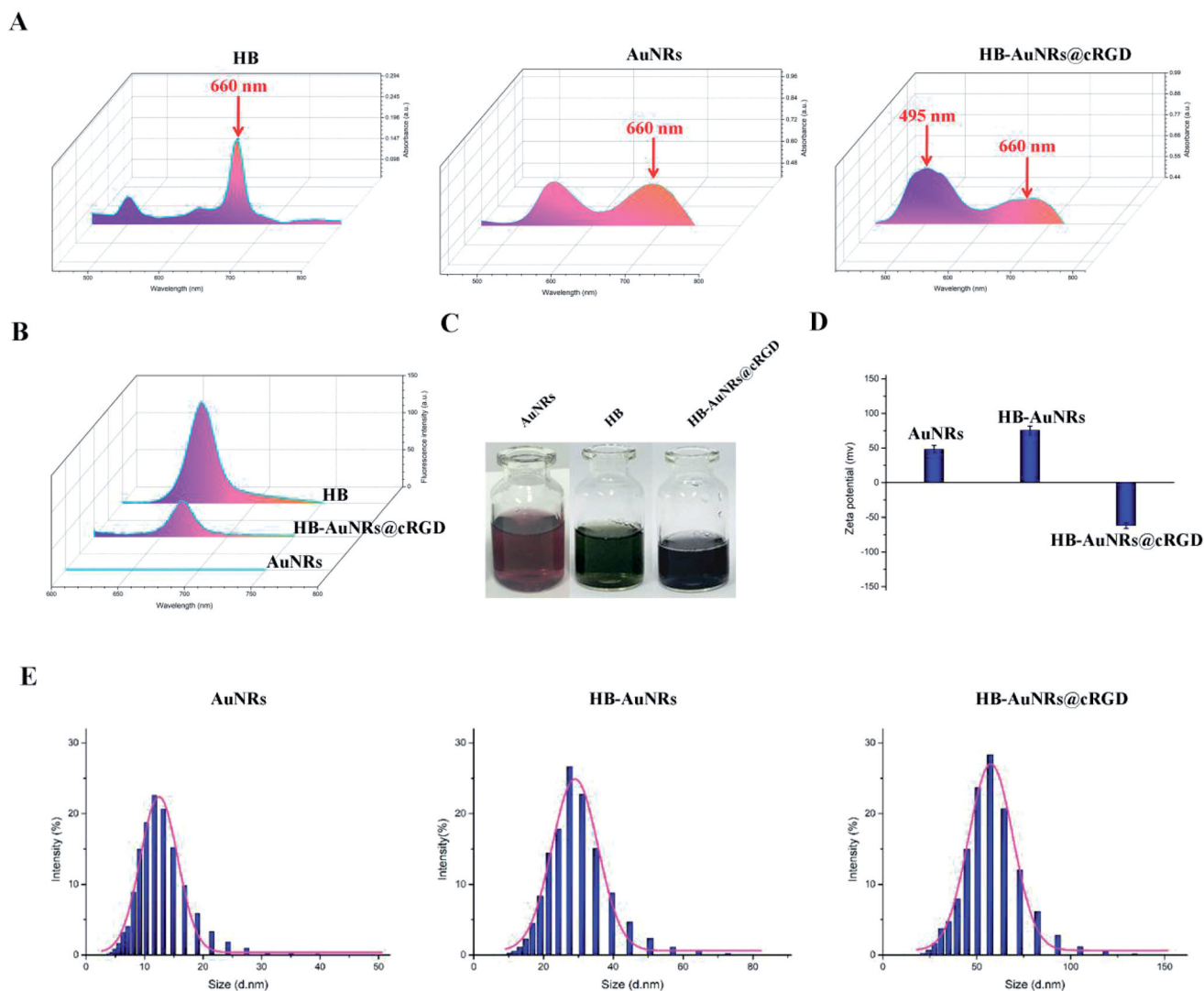


**Figure 2.** Characterization of HB-AuNRs@cRGD. (A) UV-vis spectra, (B) fluorescence emission spectra, (C) photographs, (D) surface charges (zeta-potential), and (E) size distribution of HB, AuNRs, and HB-AuNRs@cRGD.

surface of AuNRs (Figure 2(B,C)). As shown in Figure 2(D), AuNRs showed a positive surface charge ( $48.20 \pm 5.50$  mV) due to the presence of cationic surfactant CTAB. After surface functionalization with HS-PEG-NH<sub>2</sub> and HB, HB-AuNRs exhibited a positive charge ( $75.66 \pm 6.20$  mV). When cRGD was further grafted with HB-AuNRs, the surface charge of HB-AuNRs@cRGD changed from positive to negative ( $-61.60 \pm 4.31$  mV), indicating the grafting of cRGD on the surface of AuNRs. As shown in Figure 3(A), compared with the AuNRs ( $37.11 \pm 2.57$  nm), the HB-AuNRs@cRGD ( $42.73 \pm 0.51$  nm) exhibited an obvious core-shell structure, and the shell thickness on the AuNRs was approximately  $5.62 \pm 2.61$  nm. Moreover, the hydrodynamic size of HB-AuNRs@cRGD increased from  $32.75 \pm 0.21$  nm to  $68.50 \pm 1.98$  nm after sequential grafting of HB and cRGD onto the surface of AuNRs (Figure 2(E)) which was well-consistent with the AFM observations (Figure 3(B)). All above results verified the successful synthesis of HB-AuNRs@cRGD.

### 3.2. In vitro PTT and PDT efficacy evaluation

To verify the photothermal conversion ability of HB-AuNRs@cRGD, the HB-AuNRs@cRGD was irradiated upon a 660 nm laser at a power density of  $300 \text{ mW/cm}^2$  for different time periods. As shown in Figure 4(A–D)), HB-AuNRs@cRGD exhibited excellent photothermal conversion ability with a faster rate of temperature increase than AuNRs, which was attributed to the additive light absorption of HB loaded on AuNRs and the synergy between photothermal conversion ability of HB and AuNRs. To further confirm the <sup>1</sup>O<sub>2</sub> generation capability of HB-AuNRs@cRGD, DPBF was used as an <sup>1</sup>O<sub>2</sub> trapping reagent to quench its intrinsic absorbance via forming DPBF-endoperoxide complex after laser irradiation. A significant decrease of absorbance at the characteristic peak of DPBF at 415 nm was observed within 5 min, indicating the <sup>1</sup>O<sub>2</sub> generation ability of HB-AuNRs@cRGD exposure to 660 nm laser irradiation (Figure 4(E,F)). Moreover, as shown in Figure

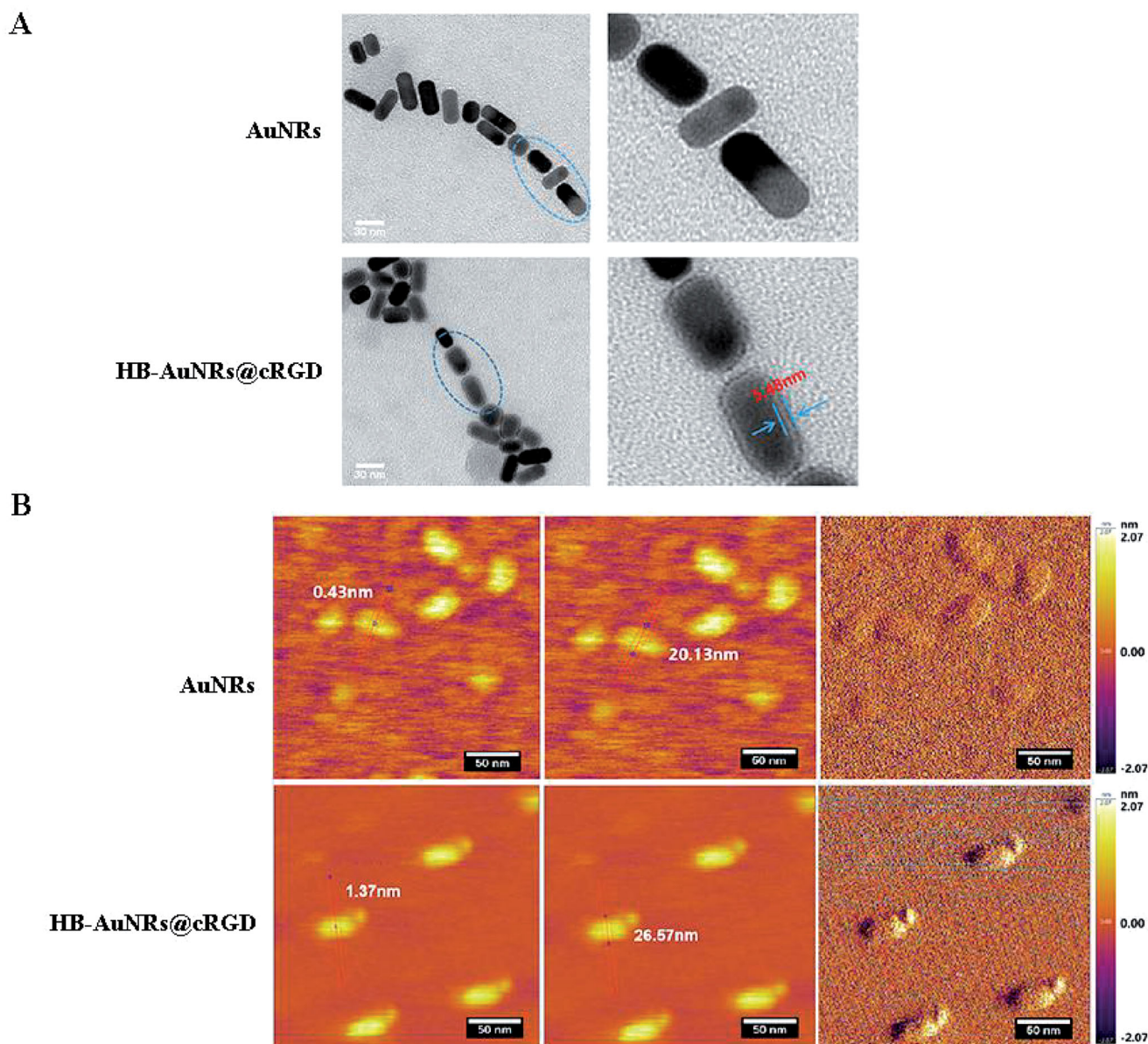


**Figure 3.** TEM and AFM images of HB-AuNRs@cRGD. (A) TEM and (B) AFM images of AuNRs and HB-AuNRs@cRGD.

4(G), AuNRs (without PEGylated) showed poor dispersity in PBS and DMEM, whereas AuNRs and HB-AuNRs@cRGD exhibited good dispersity and kept for 120 h. The result was likely due to the surface functionalization of PEG.

### 3.3. In vitro cytotoxicity evaluation

The phototherapeutic activity of AuNRs, HB, and HB-AuNRs@cRGD on ECA109 cells was evaluated by CCK-8 assay. First, ECA109 cells were incubated with AuNRs, HB, and HB-AuNRs@cRGD in the dark condition for 24 h. No obvious dark toxicity was found in ECA109 cells (Figure 5(A)), which demonstrated that all formulations exhibited biocompatibility in a certain concentration range. Upon the laser irradiation condition (660 nm, 120 mW/cm<sup>2</sup>, 168 s), all formulations showed a concentration-dependent phototoxicity. Moreover, the cell viability of ECA109 cells incubated with HB-AuNRs@cRGD nanoprobes was significantly lower than that of free AuNRs

and HB (Figure 5(B)). The remarkably increased phototoxicity of HB-AuNRs@cRGD could be explained by the fact that the production of both ROS and hyperthermia caused by the combined PDT and PTT triggered much more damage to cancer cells.

Next, both confocal microscopy imaging by calcein AM/PI co-staining (living/dead cell staining) and flow cytometry by Annexin V-FITC/PI staining were used to evaluate the death/apoptosis of cancer cells. ECA109 cells were incubated with AuNRs, HB, and HB-AuNRs@cRGD for 24 h, respectively, with or without laser radiation treatment. Upon laser irradiation conditions, the death/apoptosis ratios of cancer cells in HB-AuNRs@cRGD group were significantly stronger than the other groups (Figure 5(C–E)). The results of living/dead cell staining and Annexin V-FITC/PI staining were consistent with the CCK-8 result, indicating that HB-AuNRs@cRGD nanoprobes could be used as a promising phototherapeutic agent with powerful phototoxic potential.

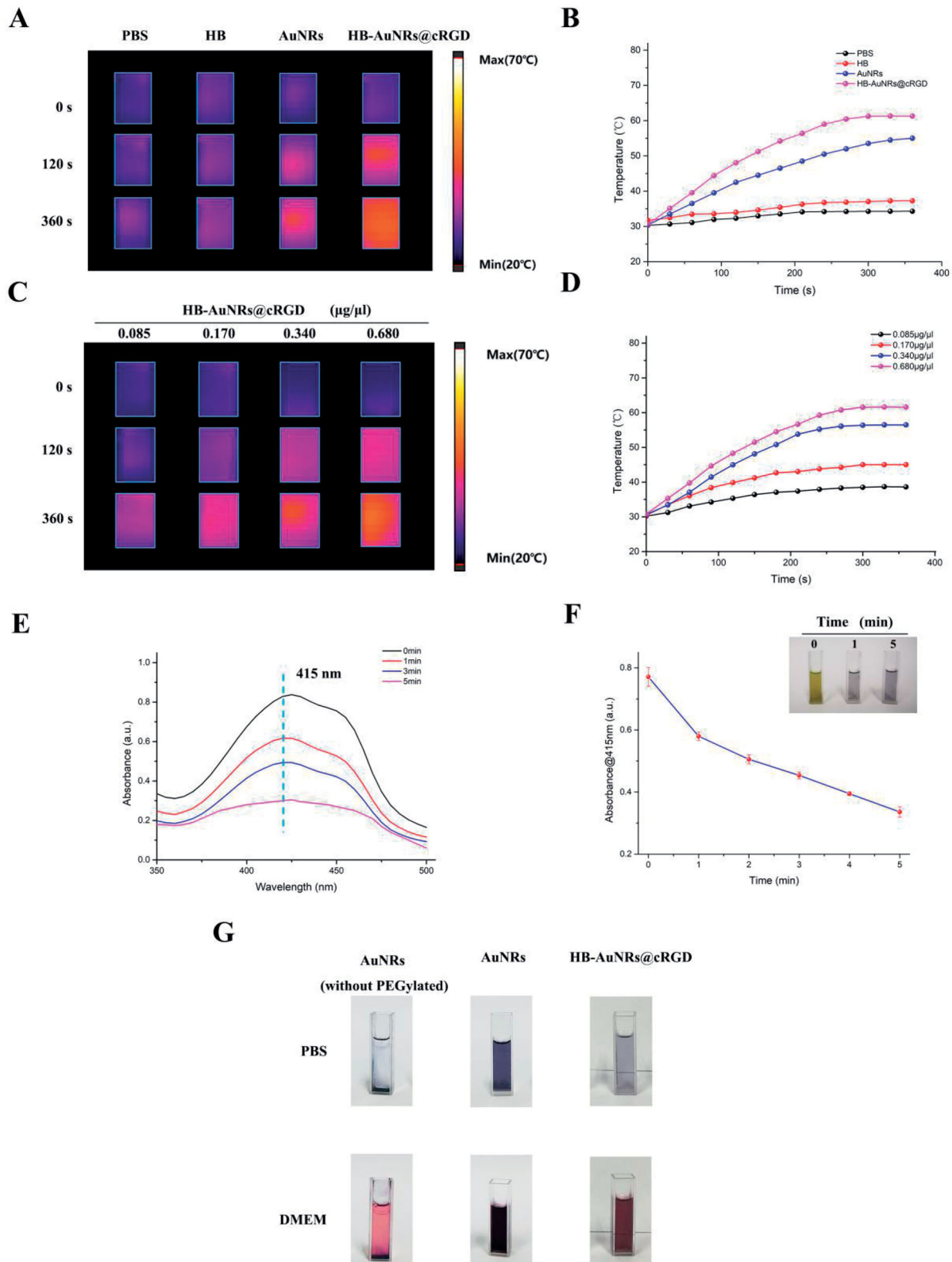


**Figure 4.** *In vitro* efficacy evaluation. (A–D) Photothermal performance of HB-AuNRs@cRGD. (A) Infrared thermographic images and (B) temperature change curves of different formulations exposure to 660 nm laser irradiation. (C) Infrared thermographic images and (D) temperature change curves of HB-AuNRs@cRGD at different concentrations exposure to 660 nm laser irradiation. (E, F) Time dependent (E) UV-vis spectra of mixture of HB-AuNRs@cRGD and DPBF, and (F) SO generation of HB-AuNRs@cRGD exposure to 660 nm laser irradiation. (G) Photographs of different formulations in PBS and DMEM.

### 3.4. *In vitro* ROS generation

To evaluate the ROS generation ability of AuNRs, HB, and HB-AuNRs@cRGD upon 660 nm laser irradiation, DCFH-DA

probe was used to monitor the generation of ROS. DCFH-DA could be hydrolyzed by intracellular esterase to produce DCFH, which could be rapidly oxidized by intracellular ROS



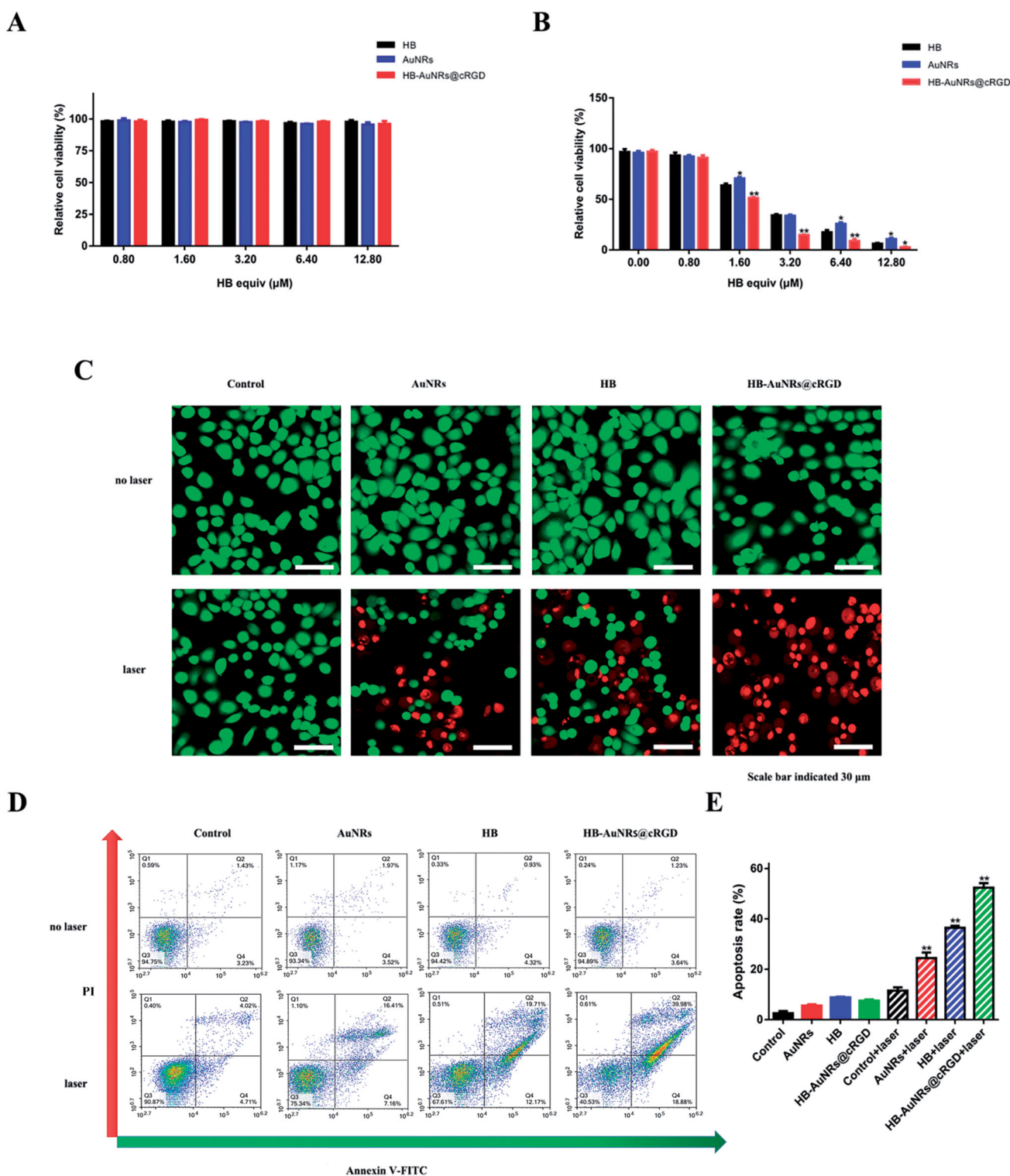


**Figure 5.** *In vitro* cytotoxicity evaluation. (A, B) Relative cell viability of ECA109 cells treated with different formulations (A) without and (B) with laser irradiation as a function of concentrations of HB. (C) CLSM images of calcein AM and PI co-stained ECA109 cells incubated with different formulations without and with laser irradiation. (D, E) Apoptosis analysis via Annexin V-FITC/PI assay of ECA109 cells incubated with different formulations without and with laser irradiation. Data are expressed as the mean ± SD ( $n = 3$ ), \* $p < .05$ , \*\* $p < .01$  vs. control.

to produce the highly fluorescent DCF (green fluorescence). As shown in Figure 6(A), the green fluorescence of DCF was observed inside ECA109 cells incubated with HB and HB-AuNRs@cRGD after laser irradiation. Moreover, the generation efficiency of ROS in ECA109 cells incubated with HB-AuNRs@cRGD was significantly higher than that of free HB

groups. The phenomenon indicated that the HB-AuNRs@cRGD could enhance the yield of intracellular ROS.

In addition, intracellular ROS often lead to mitochondrial membrane permeabilization and depolarization. Generally, the dissipation of mitochondrial membrane potential was observed in PDT-induced apoptosis (Chauhan et al., 2018).

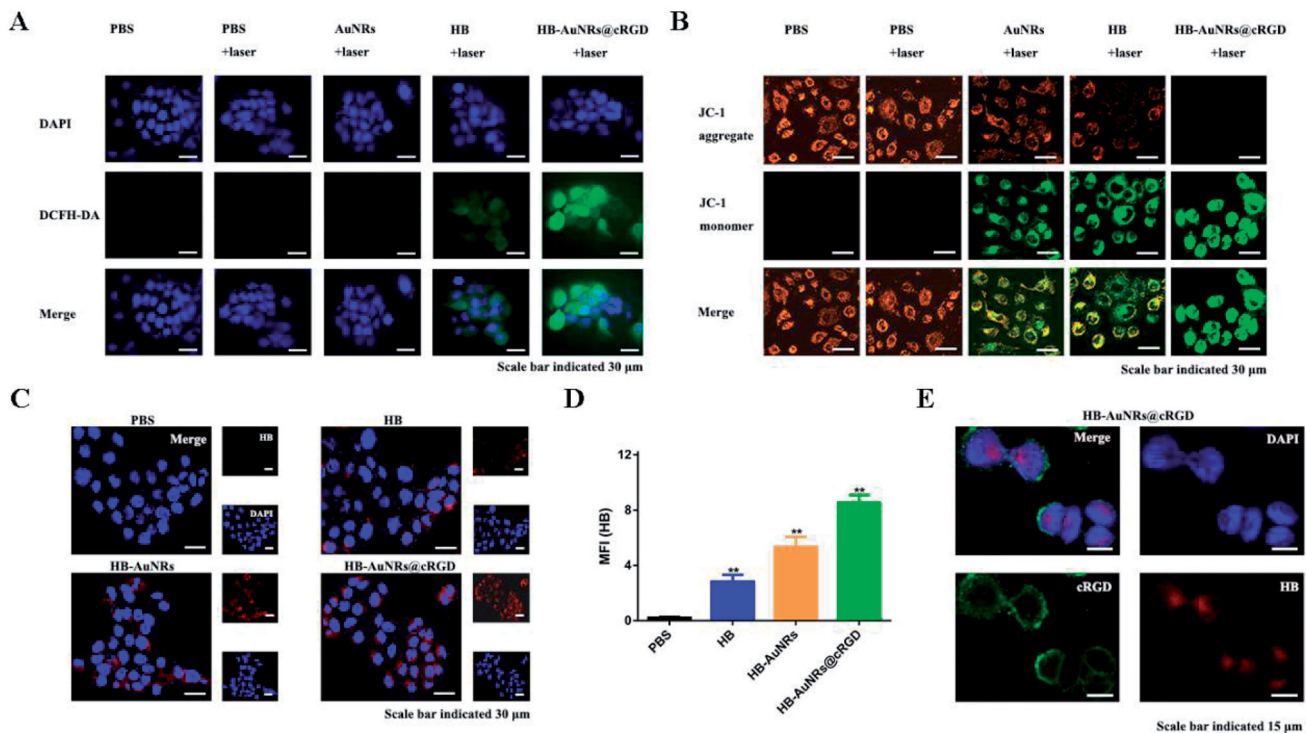


**Figure 6.** *In vitro* ROS generation, cellular uptake, and subcellular localization of ECA109 cells. (A) CLSM images of ECA109 cells incubated with different formulations using DCFH-DA under 660 nm laser irradiation for ROS generation. (B) CLSM images of ECA109 cells incubated with different formulations using JC-1 under 660 nm laser irradiation for mitochondrial membrane potential detection. (C) CLSM images of ECA109 cells incubated with PBS, HB, HB-AuNRs, and HB-AuNRs@cRGD (6.40  $\mu$ M of HB equiv.) for 24 h. (D) Mean fluorescence intensity of ECA109 cells incubated with PBS, HB, HB-AuNRs, and HB-AuNRs@cRGD (6.40  $\mu$ M of HB equiv.) for 24 h. (E) Subcellular localization of ECA109 cells incubated with HB-AuNRs@cRGD by CLSM observation.

To evaluate the alteration in mitochondrial membrane potential, JC-1 staining assay was carried out. JC-1 could accumulate in the mitochondrial matrix to form JC-1 aggregates (red fluorescence). However, when ROS induced mitochondrial membrane depolarization, JC-1 could be not assembled in the mitochondrial matrix and kept the form of JC-1 monomers (green fluorescence). Therefore, the decrease in the ratio of red (JC-1 aggregate)/green (JC-1 monomer) fluorescence intensity could reflect the mitochondria depolarization and indirectly reflect the generation of ROS. As shown in Figure 6(B), the mitochondrial depolarization of HB-AuNRs@cRGD after laser irradiation was significantly higher than that of HB. These results indicated that HB-AuNRs@cRGD after laser irradiation could produce more ROS, which in turn lead to strong PDT-induced apoptosis.

### 3.5. *In vitro* cellular uptake

To investigate the cellular uptake of photosensitizer (HB), confocal microscopy imaging was first applied to observe the internalization of esophageal cancer cell lines ECA-109 cells on all formulations. The green, red, and blue fluorescence signals respectively represented cRGD-FITC, HB, and DAPI. ECA109 cells were incubated with AuNRs, HB, and HB-AuNRs@cRGD in the dark condition for 24 h. As shown in Figure 6(C), the HB-AuNRs@cRGD nanoprobe-treated ECA109 cells showed obviously stronger red fluorescence signals compared to that of free HB and HB-AuNRs, which was well consistent with the results of mean fluorescence intensity of HB (Figure 6(D)). Moreover, as shown in Figure 6(E),

the different distribution of red fluorescence signals (HB was distributed in the cytoplasm) and green fluorescence signals (cRGD was distributed onto the membrane) indicated the intracellular release of HB photosensitizer from nanoprobe, which would be benefit for the activated PDT. Both the confocal microscopy imaging results indicated that HB-AuNRs@cRGD nanoprobe could remarkably improve the cellular uptake of photosensitizers by integrin  $\alpha$ v $\beta$ 3 receptor-mediated targeting by cRGD.

### 3.6. *In vitro* cell biological behavior evaluation

To assess the effect of nanoprobe on clonogenic ability of ECA109 cells, the colony formation assay was performed. The results showed that HB-AuNRs@cRGD with laser irradiation treatment reduced the rate of colony formation by  $8.77 \pm 3.50\%$ , which was obviously lower than HB ( $18.62 \pm 1.26\%$ ) and AuNRs ( $22.73 \pm 2.04\%$ ) groups (Figure 7(A,D)). In addition, the wound-healing assay was performed to investigate the role of nanoprobe on cancer cell migration ability of ECA109 cells. As shown in Figure 7(B,E), HB-AuNRs@cRGD with laser radiation treatment showed a more significant tendency to decrease cancer cells migration in ECA109 cells compared with the other groups. Similarly, the transwell invasion assays illustrated that HB-AuNRs@cRGD dramatically impeded the migration and invasive ability of ECA109 cells after laser irradiation compared with the other groups (Figure 7(C,F)). Notably, it could be seen that cRGD was mainly distributed on the surface of ECA-109 cancer cells (Figure 6(E)), which was due to its specific binding to integrin  $\alpha$ v $\beta$ 3 receptors on the surface esophageal cancer cells, thereby

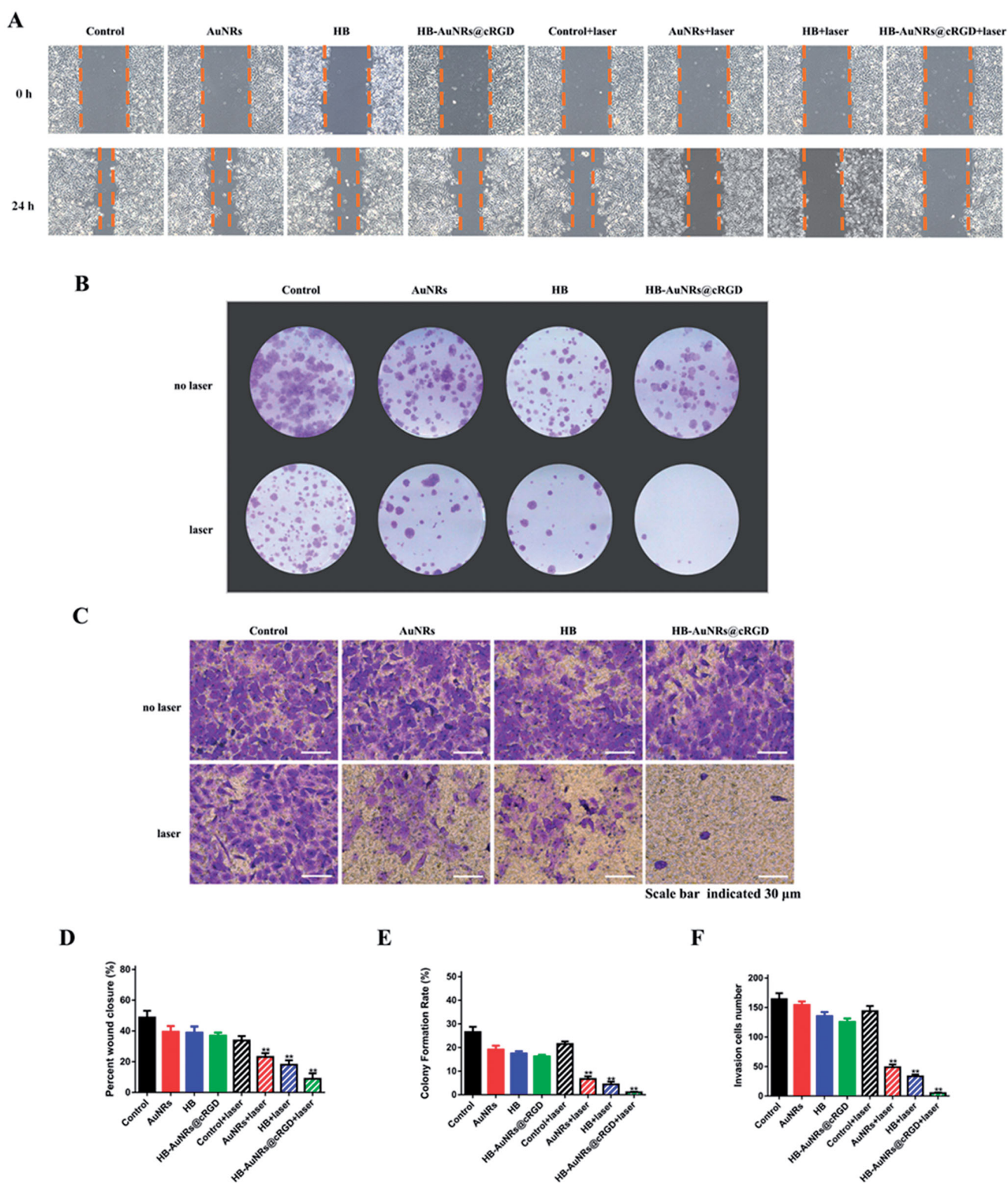


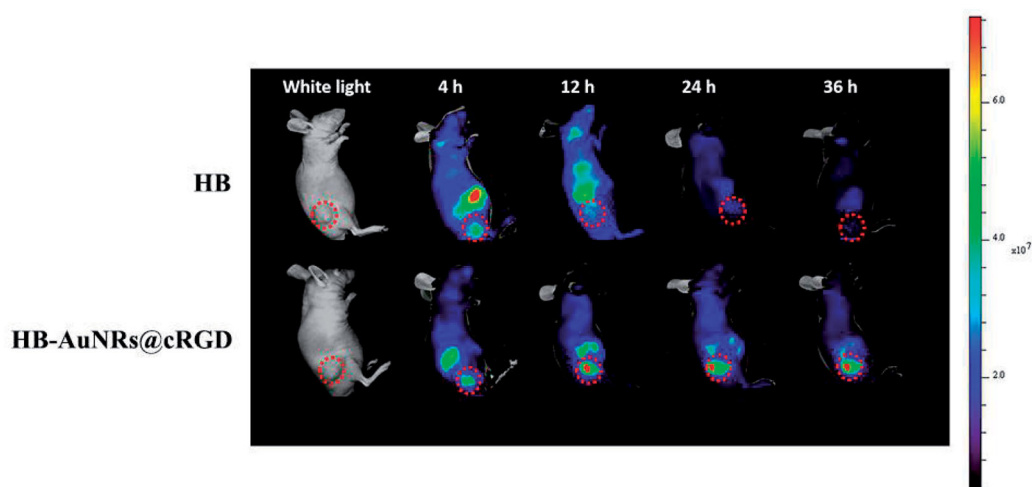
**Figure 7.** *In vitro* cell biological behavior evaluation. (A–C) Representative images of (A) wound healing assay, (B) colony formation assay, and (C) transwell invasion assay in different groups. (D–F) Quantitative analysis of (D) wound closure rate, (E) clone formation rate, and (F) invasion cells number. Data are expressed as the mean  $\pm$  SD ( $n = 3$ ),  $**p < .01$  vs. control.

inhibiting tumor cells adhesion and migration. These above results demonstrated HB-AuNRs@cRGD nanoprobe could hinder proliferation, migration, and invasion of ECA109 cells associated with the synergistic PDT/PTT.

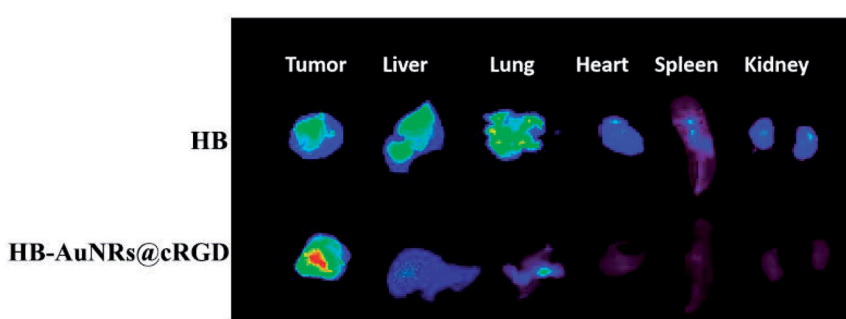
### 3.7. The bio-distribution of HB-AuNRs@cRGD

Then, we carried out the fluorescence imaging to investigate the bio-distribution of free HB and HB-AuNRs@cRGD nanoprobe in ECA109 tumor-bearing BALB/c mice. As shown in

A



B



C

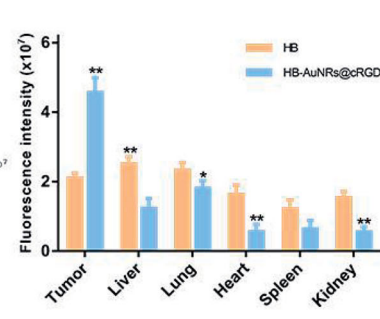


**Figure 8.** The bio-distribution of HB-AuNRs@cRGD. (A) *In vivo* fluorescent imaging of ECA109 tumor-bearing mice exposed to 660 nm laser at determined time intervals after i.v. administration of free HB and HB-AuNRs@cRGD. (B) *Ex vivo* fluorescent imaging and (C) fluorescence intensity of free HB and HB-AuNRs@cRGD in major organs and tumor tissues at 12 h after i.v. injection. Red circles indicated tumor areas. Data are expressed as the mean  $\pm$  SD ( $n = 3$ ), \* $p < .05$ , \*\* $p < .01$  vs. control.

Figure 8(A), the considerable HB fluorescence was observed in the tumor areas after 12 h post-injection of HB-AuNRs@cRGD. Moreover, the HB fluorescence located at the tumor sites of HB-AuNRs@cRGD-injected groups was significantly stronger than that of free HB-injected groups. The results implied that the tumor accumulation capacity of HB-AuNRs@cRGD was stronger than that of free HB. In addition, the fluorescence signals in the tumor areas of HB-AuNRs@cRGD-injected groups could continue for 36 h, indicating HB-AuNRs@cRGD nanoprobes possessed tumor retention effect. Next, the tumor and major organ tissues of tumor-bearing mice at 12 h post-injection were separately isolated for *ex vivo* fluorescence imaging and semi-quantitative analysis of biodistribution. As shown in Figure 8(B,C), the fluorescence signal in the tumor of HB-AuNRs@cRGD-injected group was significantly higher compared with that of free HB-injected group. However, the fluorescence signals in major organ tissues of HB-AuNRs@cRGD-injected group was significantly lower than those of free HB-injected group, especially in liver tissues. These results were well in accordance with the infrared thermal imaging result (discussed below), confirming that the HB-AuNRs@cRGD nanoprobes could preferentially accumulate in the tumor areas with long-term retention through both EPR and active binding.

### 3.8. *In vivo* infrared thermal imaging

To investigate the PTT effect of HB-AuNRs@cRGD nanoprobes *in vivo*, ECA109 tumor-bearing BALA/c mice were used for infrared thermal imaging and monitored at different time after intravenous injection. As shown in Figure 9(A,B), the tumor temperature of AuNRs-treated mice rose up to approximately 50.4°C within 500 s, while that of HB-AuNRs@cRGD-treated group increased to approximately 59.7°C. In contrast, PBS and free HB-treated groups exhibited slight temperature increase in the tumor areas under the same irradiation condition. The results indicated that HB-AuNRs@cRGD could effectively accumulate at the tumor sites, and produced hyperthermia to kill the cancer cells after laser irradiation. Moreover, the significantly improved enrichment of HB-AuNRs@cRGD at the tumor sites contributed to the significantly stronger PTT performance compared with free AuNRs.

### 3.9. *In vivo* anti-tumor effect investigation

The anti-tumor effects of free HB, AuNRs, and HB-AuNRs@cRGD without/with different laser irradiation (660 nm, 200 mW/cm<sup>2</sup>, 500 s) were performed to investigate the tumor growth inhibition effect. The digital photographs of mice

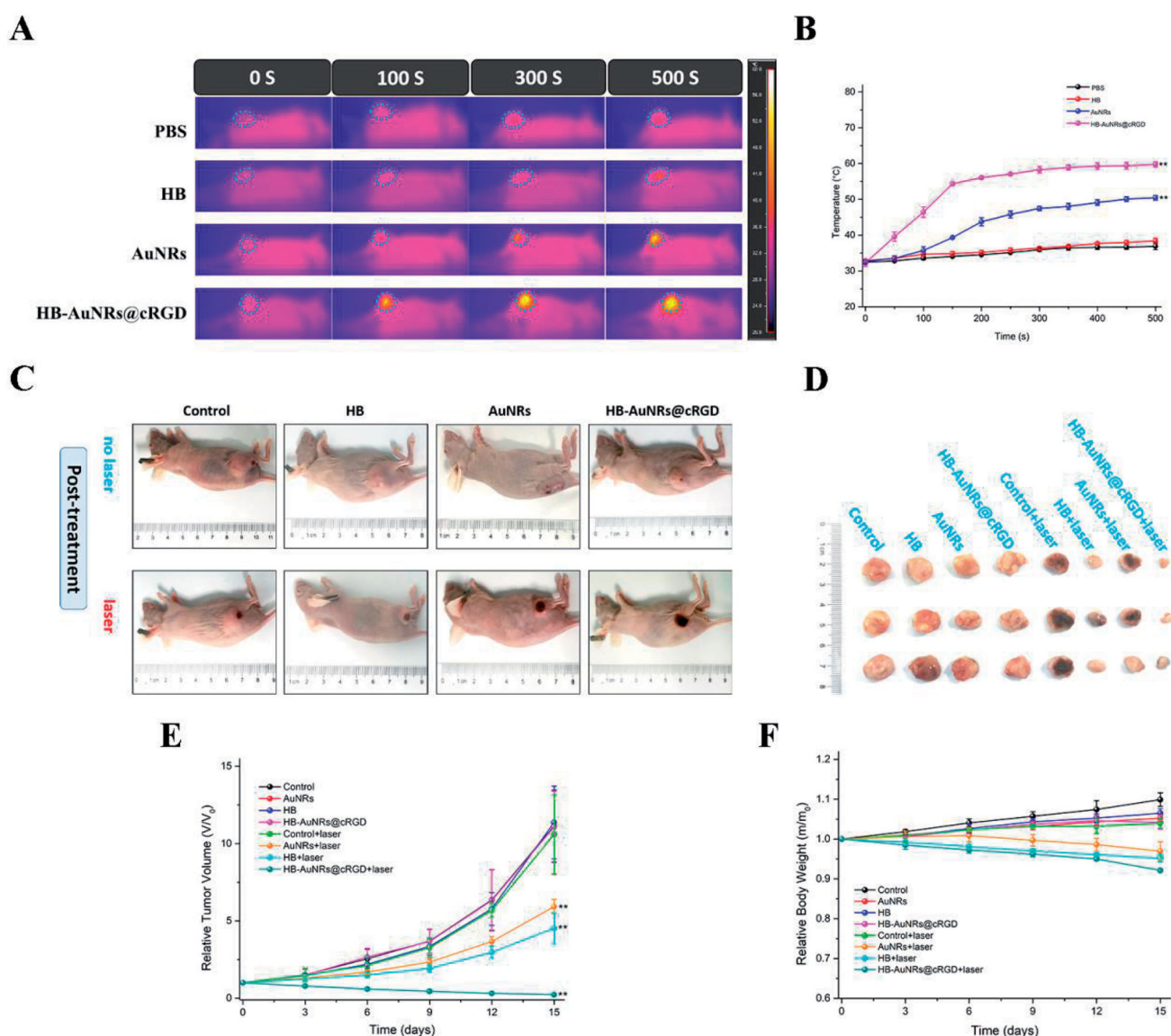


**Figure 9.** *In vivo* infrared thermal imaging and anti-tumor effect. (A) Infrared thermographic images of tumor-bearing mice under 660 nm laser irradiation for 0, 100, 300, and 500 s. Laser was irradiated at 12 h post i.v. injection of formulations. (B) Temperature variation curve at tumor sites after different treatment. (C) Representative photographs of ECA109 tumor-bearing mice from different groups during 15 days after treatment. (D) Photographs of sacrificed tumors from different groups during 15 days after treatment. (E) Tumor growth curves and (F) body weight change of ECA109 tumor-bearing mice from different groups during 15 days after treatment. Tumor volumes and body weight were normalized to their initial sizes and weight. Error bars represented the standard deviations of 6–8 mice per group,  $**p < .01$  vs. control.

and tumor tissues of each group were recorded at the 15th day during the treatment (Figure 9(C,D)). The volume of tumors was measured every three days, and then the tumor volume was plotted as a function of time (Figure 9(E)). For PBS (control group), HB, AuNRs, and HB-AuNRs@cRGD without laser irradiation, the tumors grew rapidly. The similar phenomenon was observed in PBS with laser irradiation, which illustrated that the photosensitizer or laser irradiation alone could not inhibit tumors growth. Remarkably, the enhanced tumor therapeutic effect was observed in the HB-AuNRs@cRGD group with laser irradiation, which was significantly stronger than the HB and AuNRs with laser irradiation. Moreover, H&E stains of tumor sections were collected from PBS and HB-AuNRs@cRGD with/without laser irradiation on 15 days post-treatment. As shown in Figure 10(A), the

significant tumor cell damage with nuclear membrane fragmentation (karyorrhexis) and nuclei shrinkage with pyknosis (the irreversible condensation of chromatin) was observed from tumor tissues in HB-AuNRs@cRGD group with laser irradiation, which could lead to intensive necrosis or apoptosis. Nevertheless, the tumor cells in PBS group exhibited a tightly arranged structure and vigorous proliferation. These results suggested that HB-AuNRs@cRGD under 660 nm laser irradiation exhibited excellent anti-tumor effects on tumors.

### 3.10. The biosafety evaluation of HB-AuNRs@cRGD

To gain insight into the biosafety of HB-AuNRs@cRGD nanoparticles, major organs were collected from PBS and HB-

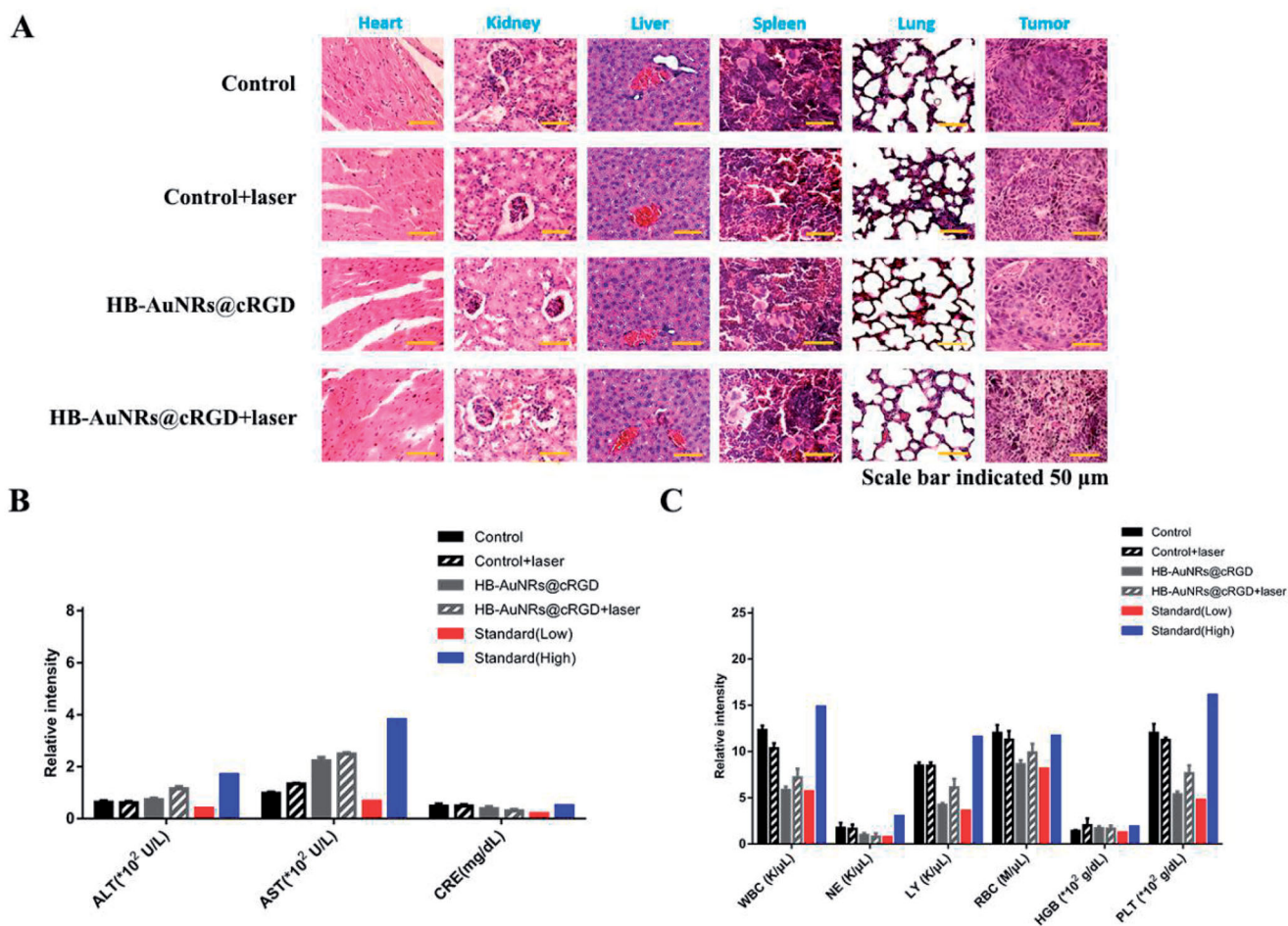


**Figure 10.** *In vivo* biosafety assessment. (A) H&E stained images of major organs and tumor tissue sections collected from different treatment groups on 15 days post-treatment. (B) The aspartate transaminase (AST), alanine aminotransferase (ALT), blood creatinine (CRE) analysis in the serum, and (C) the hematological parameters of the mice collected from different treatment groups on 15 days post-treatment. Error bars represented the standard deviations of three mice per group.

AuNRs@cRGD with/without laser irradiation on 15 days post-treatment for HE staining analysis (Figure 10(A)). The major organ tissues in each group exhibited normal cells tightly arranged with intact shape, indicating no significant acute toxicity of formulation or laser irradiation. Next, blood samples of mice on 15 days post-treatment were collected for serum chemistry and blood cell analysis. No obvious abnormality in the main serum enzyme content, creatinine and blood cell counts was observed in Figure 10(B,C). Furthermore, no obvious fluctuation in mice body weight was found in all groups (Figure 9(F)). These results indicated that HB-AuNRs@cRGD nanoprobe exhibited ideal biosafety and potential for clinical transformation.

### 3.11. The advantages of HB-AuNRs@cRGD

In previous studies, some AuNRs-based nanoprobe were applied to PTT/PDT of cancer. Zhang et al. reported a 4-carboxyphenyl porphyrin-conjugated silica coated AuNR (AuNR@SiO<sub>2</sub>-TCPP) with almost 180 nm diameter for PTT/PDT of lung cancer, which needed to be activated by 660 nm and 808 nm lasers. *In vitro*, the A549 cell inhibition rate was less than 80% (Zhang et al., 2019). Liu et al. constructed a pegylated mesoporous SiO<sub>2</sub> coated AuNRs for entrapping

photosensitizer Ce6 and d-CPP (Ce6-AuNR@SiO<sub>2</sub>d-CPP) with almost 170 nm diameter. Ce6-AuNR@SiO<sub>2</sub>d-CPP could be used for PTT/PDT of breast cancer with 650 nm and 808 nm lasers irradiation (Liu et al., 2018a). Wang et al. synthesized a AuNR conjugated with rose bengal (RB-GNRs), exhibiting PDT/PTT synergistic effects against oral cancer when illuminated by 532 nm and 810 nm lasers. However, RB-GNRs might present stronger dark toxicity as the concentration enhanced (Wang et al., 2014).

In this study, we constructed a novel therapeutic nanoprobe for PDT/PTT of esophageal cancer composed of HB and AuNRs, further grafted with tumor-targeting peptide cRGD (HB-AuNRs@cRGD). Compared with other AuNRs-based nanoprobe, HB-AuNRs@cRGD possessed smaller size (almost 70 nm diameter) and better biocompatibility with more concise synthesis process. In addition, our previous study first reported that a new type of second-generation photosensitizer HB was a monomer with clearer chemical structure and higher purity ( $\geq 99\%$ ) compared with other clinical photosensitizers. Moreover, the absorption coefficient of HB at the optimal UV-vis absorption wavelength (660 nm) was significantly improved ( $\epsilon \geq 10^4 \text{ M}^{-1} \text{ cm}^{-1}$ ), thereby further raising the tissue infiltration depth of laser (Liu et al., 2020). In particular, our nanoprobe exhibited stronger phototoxicity

(almost 95% of cell inhibition rate) with lower biotoxicity, due to the advanced physiochemical characteristics, superior photodynamic efficacy, and high biosafety of HB. Benefited from the EPR effect and active binding of cRGD, HB-AuNRs@cRGD presented an increased tumor homing and cellular uptake with 2.0-fold absorption property vs. free HB. Different from the traditional combination of PDT and PTT activated by two separate lasers, HB-AuNRs@cRGD nanoprobes would simultaneously produce ROS and hyperthermia excited by a single 660 nm NIR laser, thereby synergistically improving antitumor efficiency and effectively inhibiting tumor growth (almost 80% of tumor inhibition rate) without obvious acute side effects. This promising strategy for single NIR laser-induced and imaging-guided targeted combination phototherapy avoided the prolongation of treatment time and the complication of therapeutic process, presenting enormous potential for clinical application of esophageal cancer therapy.

#### 4. Conclusions

We had developed a self-imaging and tumor-targeting nano-drug to significantly improve the PDT/PTT effect. By chemically coupling HB and cRGD to PEG-functionalized AuNRs via an amide bond ( $-\text{NH}=\text{CO}-$ ), PDT and PTT were integrated into one therapeutic system (HB-AuNRs@cRGD). The PEG modified on HB-AuNRs@cRGD could prolong the blood half-life, and the loaded cRGD could improve the tumor-targeting ability. Under a single 660 nm laser irradiation, the HB-AuNRs@cRGD could preferentially accumulate in the tumor areas and achieve a powerful killing effect on ECA109 cells by simultaneously producing both significant ROS and hyperthermia. In addition, the HB-AuNRs@cRGD exhibited excellent phototherapeutic efficacy in the subcutaneous esophageal cancer models, the tumor growth was significantly inhibited. Our tumor-targeting phototherapeutic nanodrugs showed a potential prospect in single NIR laser-induced PDT/PTT under the guidance of fluorescence imaging. We believed that HB-AuNRs@cRGD might be promising as a effective tumor theranostic platform.

#### Acknowledgements

The authors thank Haining Lvsheng Pharmaceutical Technology Co., Ltd. for providing the LS-HB.

#### Disclosure statement

The authors declare no competing financial interest.

This study received approval from Xiamen university ethics committees (XMULAC20170297).

#### Funding

This work was financially supported by the National Natural Science Foundation of China [81773770], and the Provincial Public Welfare Project of Fujian Province [2019R1001-2, 2020R1001001].

#### References

- Baldea I, Olteanu DE, Bolfa P, et al. (2016). Melanogenesis and DNA damage following photodynamic therapy in melanoma with two meso-substituted porphyrins. *J Photochem Photobiol B* 161:402–10.
- Bertrand N, Wu J, Xu X, et al. (2014). Cancer nanotechnology: the impact of passive and active targeting in the era of modern cancer biology. *Adv Drug Deliv Rev* 66:2–25.
- Camerin M, Moreno M, Marin MJ, et al. (2016). Delivery of a hydrophobic phthalocyanine photosensitizer using PEGylated gold nanoparticle conjugates for the in vivo photodynamic therapy of amelanotic melanoma. *Photochem Photobiol Sci* 15:618–25.
- Chauhan DS, Prasad R, Devrukhkar J, et al. (2018). Disintegrable NIR light triggered gold nanorods supported liposomal nanohybrids for cancer theranostics. *Bioconjug Chem* 29:1510–8.
- Cheng L, Wang C, Feng L, et al. (2014). Functional nanomaterials for phototherapies of cancer. *Chem Rev* 114:10869–939.
- Danhier F, Le Breton A, Preat V. (2012). RGD-based strategies to target  $\alpha(v)\beta(3)$  integrin in cancer therapy and diagnosis. *Mol Pharm* 9:2961–73.
- Denkova AG, de Kruijff RM, Serra-Crespo P. (2018). Nanocarrier-mediated photochemotherapy and photoradiotherapy. *Adv Healthc Mater* 7:e1701211.
- Donohoe C, Senge MO, Arnaut LG, Gomes-da-Silva LC. (2019). Cell death in photodynamic therapy: from oxidative stress to anti-tumor immunity. *Biochim Biophys Acta Rev Cancer* 1872:188308.
- Fan Z, Chang Y, Cui C, et al. (2018). Near infrared fluorescent peptide nanoparticles for enhancing esophageal cancer therapeutic efficacy. *Nat Commun* 9:2605.
- Gajbhiye KR, Gajbhiye V, Siddiqui IA, Gajbhiye JM. (2019). cRGD functionalised nanocarriers for targeted delivery of bioactives. *J Drug Target* 27:111–24.
- Gui C, Cui DX. (2012). Functionalized gold nanorods for tumor imaging and targeted therapy. *Cancer Biol Med* 9:221–33.
- Hamzah J, Kotamraju VR, Seo JW, et al. (2011). Specific penetration and accumulation of a homing peptide within atherosclerotic plaques of apolipoprotein E-deficient mice. *Proc Natl Acad Sci U S A* 108:7154–9.
- Huang HC, Rege K, Heys JJ. (2010). Spatiotemporal temperature distribution and cancer cell death in response to extracellular hyperthermia induced by gold nanorods. *ACS Nano* 4:2892–900.
- Kalyane D, Raval N, Maheshwari R, et al. (2019). Employment of enhanced permeability and retention effect (EPR): nanoparticle-based precision tools for targeting of therapeutic and diagnostic agent in cancer. *Mater Sci Eng C Mater Biol Appl* 98:1252–76.
- Kennedy LC, Bickford LR, Lewinski NA, et al. (2011). A new era for cancer treatment: gold-nanoparticle-mediated thermal therapies. *Small* 7:169–83.
- Kim M, Sahu A, Kim GB, et al. (2018). Comparison of in vivo targeting ability between cRGD and collagen-targeting peptide conjugated nano-carriers for atherosclerosis. *J Control Release* 269:337–46.
- Kwiatkowski S, Knap B, Przystupski D, et al. (2018). Photodynamic therapy – mechanisms, photosensitizers and combinations. *Biomed Pharmacother* 106:1098–107.
- Li B, Wang F, Gui L, et al. (2018). The potential of biomimetic nanoparticles for tumor-targeted drug delivery. *Nanomedicine* 13:2099–118.
- Li W, Zhang H, Guo X, et al. (2017). Gold nanospheres-stabilized indocyanine green as a synchronous photodynamic–photothermal therapy platform that inhibits tumor growth and metastasis. *ACS Appl Mater Interfaces* 9:3354–67.
- Li X, Lovell JF, Yoon J, Chen X. (2020). Clinical development and potential of photothermal and photodynamic therapies for cancer. *Nat Rev Clin Oncol* 17:657–74.
- Li Z, Huang P, Zhang X, et al. (2010). RGD-conjugated dendrimer-modified gold nanorods for in vivo tumor targeting and photothermal therapy. *Mol Pharm* 7:94–104.
- Lino RLB, Dos Santos PK, Pisani GFD, et al. (2019). Alphavbeta3 integrin blocking inhibits apoptosis and induces autophagy in murine breast tumor cells. *Biochim Biophys Acta Mol Cell Res* 1866:118536.

- Liu C, Wu T, Wang S, et al. (2020). Anticancer effect of LS-HB-mediated photodynamic therapy on hepatocellular carcinoma in vitro and in vivo. *Photodiagn Photodyn Ther* 30:101718.
- Liu L, Xie HJ, Mu LM, et al. (2018a). Functional chlorin gold nanorods enable to treat breast cancer by photothermal/photodynamic therapy. *Int J Nanomedicine* 13:8119–35.
- Liu M, Zheng C, Cui M, et al. (2018b). Graphene oxide wrapped with gold nanorods as a tag in a SERS based immunoassay for the hepatitis B surface antigen. *Mikrochim Acta* 185:458.
- Liu Y, Crawford BM, Vo-Dinh T. (2018c). Gold nanoparticles-mediated photothermal therapy and immunotherapy. *Immunotherapy* 10: 1175–88.
- Mehraban N, Freeman HS. (2015). Developments in PDT sensitizers for increased selectivity and singlet oxygen production. *Materials* 8: 4421–56.
- Melancon MP, Zhou M, Li C. (2011). Cancer theranostics with near-infrared light-activatable multimodal nanoparticles. *Acc Chem Res* 44: 947–56.
- Miller SE, Veale RB. (2001). Environmental modulation of alpha(v), alpha(2) and beta(1) integrin subunit expression in human oesophageal squamous cell carcinomas. *Cell Biol Int* 25:61–9.
- Mioc A, Mioc M, Ghiulai R, et al. (2019). Gold nanoparticles as targeted delivery systems and theranostic agents in cancer therapy. *Curr Med Chem* 26:6493–513.
- Mohammadi Z, Sazgarnia A, Rajabi O, et al. (2013). An in vitro study on the photosensitivity of 5-aminolevulinic acid conjugated gold nanoparticles. *Photodiagn Photodyn Ther* 10:382–8.
- Ruoslahti E, Bhatia SN, Sailor MJ. (2010). Targeting of drugs and nanoparticles to tumors. *J Cell Biol* 188:759–68.
- Tanaka Y, Mimori K, Shiraishi T, et al. (2000). alpha6 integrin expression in esophageal carcinoma. *Int J Oncol* 16:725–9.
- Tian B, Wang C, Zhang S, et al. (2011). Photothermally enhanced photodynamic therapy delivered by nano-graphene oxide. *ACS Nano* 5: 7000–9.
- Wang B, Wang JH, Liu Q, et al. (2014). Rose-bengal-conjugated gold nanorods for in vivo photodynamic and photothermal oral cancer therapies. *Biomaterials* 35:1954–66.
- Wang F, Li Y, Shen Y, et al. (2013a). The functions and applications of RGD in tumor therapy and tissue engineering. *Int J Mol Sci* 14: 13447–62.
- Wang S, Huang P, Nie L, et al. (2013b). Single continuous wave laser induced photodynamic/plasmonic photothermal therapy using photosensitizer-functionalized gold nanostars. *Adv Mater* 25:3055–61.
- Weber MR, Zuka M, Lorger M, et al. (2016). Activated tumor cell integrin alphavbeta3 cooperates with platelets to promote extravasation and metastasis from the blood stream. *Thromb Res* 140 Suppl.1:S27–S36.
- Xiao Q, Zheng X, Bu W, et al. (2013). A core/satellite multifunctional nanotheranostic for in vivo imaging and tumor eradication by radiation/photothermal synergistic therapy. *J Am Chem Soc* 135:13041–8.
- Xu H, Liu C, Mei J, et al. (2012a). Effects of light irradiation upon photodynamic therapy based on 5-aminolevulinic acid–gold nanoparticle conjugates in K562 cells via singlet oxygen generation. *Int J Nanomedicine* 7:5029–38.
- Xu W, Luo T, Li P, et al. (2012b). RGD-conjugated gold nanorods induce radiosensitization in melanoma cancer cells by downregulating alpha(v)beta(3) expression. *Int J Nanomedicine* 7:915–24.
- Yang K, Feng L, Shi X, Liu Z. (2013). Nano-graphene in biomedicine: theranostic applications. *Chem Soc Rev* 42:530–47.
- Yang S, Chen C, Qiu Y, et al. (2021). Paying attention to tumor blood vessels: cancer phototherapy assisted with nano delivery strategies. *Biomaterials* 268:120562.
- Zhang S, Lv H, Zhao J, et al. (2019). Synthesis of porphyrin-conjugated silica-coated Au nanorods for synergistic photothermal therapy and photodynamic therapy of tumor. *Nanotechnology* 30:265102.
- Zheng Y, Ji S, Czerwinski A, et al. (2014). FITC-conjugated cyclic RGD peptides as fluorescent probes for staining integrin  $\alpha v \beta 3 / \alpha v \beta 5$  in tumor tissues. *Bioconjug Chem* 25:1925–41.